Predicting Hydrogen-Assisted Crack Initiation in Stretch-Formed AHSS Through a Coupled Diffusion—Mechanics Model and Process Window Map

 $H.~Kuo^{1,*}~and~J.~Chen^1$

¹Ohio Northern University, Ada, Ohio, USA

(Received: 25 January 2025. Received in revised form: 18 March 2025. Accepted: 11 May 2025. Published online: 30 June 2025.)

Abstract

Hydrogen-assisted cracking in advanced high-strength steels (AHSS) during or after stretch forming remains a critical barrier to lightweight automotive design. We present a predictive framework that couples finite-strain elastoplastic mechanics with trap-dominated hydrogen diffusion, accounts for stress-driven transport and strain-induced microstructural evolution, and is calibrated against operando/ ex-situ measurements of residual stress, plasticity proxies, and phase fraction. The model correctly predicts the experimentally observed first-crack locus at the foot/hillside region and reproduces the dependence of initiation on stretch height and charging severity. Using the validated model, we construct a process window map—a practitioner-ready diagram in the space of punch stroke, punch radius, and friction coefficient—that separates safe, delayed, and fast-crack regimes. The map yields quantitative guidance for tooling/lubrication choices and forms the basis for a pass/fail screening rule via a normalized risk index. This work operationalizes mechanism into design rules that can be deployed in forming process development.

Keywords: hydrogen embrittlement, AHSS, diffusion-trap model, stress-assisted transport, finite element, process map

1. Introduction

Advanced high-strength steels (AHSS) with transformation-induced plasticity (TRIP) and martensite-aided microstructures enable significant weight reduction in automotive body-in-white components by combining high ultimate strength with useful uniform elongation. However, under specific manufacturing and service environments these grades remain vulnerable to hydrogen-assisted cracking (HAC). In stretch-forming operations, the contact geometry and frictional constraints concentrate circumferential (hoop) tensile stresses at the punch foot and adjacent hillside region. Elevated hydrostatic tension, together with strain localization and strain-induced phase transformation, creates preferential pathways for hydrogen ingress and trapping, which in turn lowers the local resistance to crack nucleation and accelerates subcritical crack growth [1–3].

Hydrogen embrittlement mechanisms relevant to AHSS include (i) hydrogen-enhanced localized plasticity (HELP), which lowers barriers for dislocation motion and promotes strain localization; (ii) hydrogen-enhanced decohesion (HEDE), which reduces cohesive strength at interfaces and ahead of crack tips; and (iii) effects arising from microstructural evolution, such as strain-induced martensitic transformation that alters both mechanical fields and the spectrum/density of trapping sites [4–6]. In TRIP-aided martensitic steels, retained austenite (RA) transforms under strain, typically raising strength but also modifying hydrogen diffusivity, solubility, and trap kinetics in a spatially heterogeneous manner. Consequently, the relevant state variables are coupled: plastic strain and phase fraction feed back to the mechanical response, alter trap density and binding energy distribution, and shift the effective hydrogen transport parameters [7].

Prior experimental work has mapped residual and applied stress fields in stretch-formed geometries using energy-dispersive X-ray diffraction (ED-XRD), characterized plasticity through peak-broadening metrics (e.g., FWHM), quantified RA evolution (f_{γ}), and monitored crack initiation timing and location during or after electrochemical charging [8,9]. These studies consistently report first-crack initiation near the foot/hillside under hydrogen charging and highlight the role of hoop tension and plastic strain as predictors. Yet, practitioners still lack: (a) a predictive forward model that ingests a proposed tool/processing setup and returns the likely crack initiation locus and time-to-initiation; and (b) an actionable process window that translates mechanism into simple design rules over stroke, punch radius, and friction (or lubricant choice). Existing guidelines often remain empirical, geometry-specific, and difficult to generalize beyond the tested conditions.

Predictive modeling must address (1) finite-strain elastoplasticity under large deformations with contact and friction; (2) trap-dominated, stress-assisted hydrogen diffusion, including hydrostatic-stress-driven flux terms and concentration-stress coupling; (3) evolution of trap density $N_t(\bar{\varepsilon}^p$, phase) and effective diffusivity/solubility as plastic strain accumulates and RA transforms; (4) reliable boundary conditions for hydrogen ingress under charging, including reduced exchange in lubricated or shielded contact zones; and (5) calibration against heterogeneous, multi-modal data (stress maps, plasticity proxies,

^{*}Corresponding author (h.kou@gmail.com)

phase fraction, and crack onset). While each element has prior art, an integrated, validated framework tailored to stretch forming of AHSS is not yet standard practice in process design [10].

Automotive forming lines require quick decisions on tooling and lubrication to meet dimensional targets while avoiding delayed fracture. A map that delineates Safe (no crack within the relevant observation window), Delayed (initiation after a tolerable dwell), and Fast (early initiation) regimes in terms of punch stroke h, punch radius R_p , and friction coefficient μ would provide immediate, plant-level utility. Such a map is only defensible if underpinned by a model that reproduces measured fields and outcomes, and if its boundaries can be summarized by a compact index suitable for supplier screening [11].

This work advances two linked objectives:

- 1. Develop a coupled diffusion—mechanics finite element (FE) model for stretch forming of AHSS that predicts the first-crack locus and time under hydrogen charging, by combining finite-strain plasticity, stress-assisted hydrogen transport, and trap kinetics tied to plasticity and phase transformation.
- 2. Convert model predictions into an actionable process window map over (h, μ, R_p) and distill a normalized risk index \mathcal{R} that separates Safe/Delayed/Fast regimes with high fidelity.

Our central hypothesis is that the intersection of two level sets—peak hoop tension $\sigma_{\theta\theta,\text{max}}$ at the foot/hillside and local diffusible hydrogen C_{H} (as shaped by stress-driven flux and trap dynamics)—governs crack initiation timing. We further hypothesize that moderate reductions in μ or increases in R_p shift $\sigma_{\theta\theta,\text{max}}$ and the residence time of high hydrostatic tension sufficiently to move operating points from Fast/Delayed into Safe without compromising formability.

The present model focuses on diffusible hydrogen under isothermal conditions and an effective single (or few) trap family parameterization. Edge damage from trimming/shearing and coatings with complex uptake kinetics are outside the primary scope but are compatible with the framework as future extensions. Calibration uses independent datasets (ED-XRD stress, FWHM, f_{γ} , and thermal desorption spectroscopy for total diffusible hydrogen) rather than tuning to crack timing alone, to preserve predictive validity.

We make four contributions:

- 1. A coupled mechanics—diffusion FE formulation with stress-assisted flux and trap kinetics, linked to strain and RA evolution, implemented within a robust staggered solution strategy.
- 2. A data-calibrated model that reproduces (i) the experimentally observed first-crack locus at the foot/hillside and (ii) the dependence of time-to-initiation on stroke and charging severity across validation conditions.
- 3. A practitioner-ready process window map in the (h, μ, R_p) space, identifying Safe/Delayed/Fast regions and quantifying how modest changes in tooling/lubrication move operating points to safety.
- 4. A compact, normalized risk index \mathcal{R} with a pass/fail threshold $\mathcal{R}_{\text{crit}}$ derived from logistic fits to simulation–experiment labels, enabling supplier screening without full-field measurements.

Section 2 formulates the mechanics-diffusion-trap model, boundary conditions, and calibration protocol. Section 3 validates predictions against measured fields and initiation data, explores sensitivities to (h, μ, R_p) , and constructs the process window map and risk index. Section 4 discusses implications, limitations, and integration into forming workflows, and Section 5 summarizes key outcomes and opportunities for extension (e.g., edge damage and coating effects).

2. Methods

2.1 Geometry, material, and loading

We model the hemispherical punch stretch-forming test of a square TM (TRIP-aided martensitic) steel coupon measuring $50 \times 50 \times 1.2$ mm, matching the experimental setup. A hemispherical punch of radius $R_p = 8.5$ mm indents the sheet at a crosshead speed of 1 mm/min. Two punch strokes are reproduced: h = 6 mm and h = 8 mm, which produced stretch heights H = 6.28 mm and H = 8.02 mm, respectively, and peak loads of approximately 35 kN (for 6 mm) and 40 kN (for 8 mm). A graphite-type lubricant was applied on the punch-sheet interface.

Axisymmetry is assumed, and a refined quadratic mesh is employed in the top, foot, hillside, and plain regions with geometric grading toward the foot radius. The blank holder/clamp is modeled using kinematic constraints, and punch—sheet contact follows Coulomb friction with coefficient μ , which is treated as a calibration parameter against the measured load—stroke curves.

Material law (mechanics). The matrix follows finite-strain J_2 plasticity with isotropic hardening $\sigma_y(\bar{\epsilon}^p)$ calibrated to the measured monotonic properties of the as-heat-treated sheet: yield strength (0.2% proof) 949 MPa, tensile strength 1404 MPa, uniform elongation 5.1%, and total elongation 8.7%. Strain-induced martensitic transformation is included via a kinetic law for the retained-austenite fraction f_{γ} :

$$\dot{f}_{\gamma} = -k_0 \exp\left(-\frac{Q}{k_{\rm B}T}\right) g(\bar{\varepsilon}^p, \dot{\bar{\varepsilon}}^p) f_{\gamma},\tag{1}$$

where $g(\cdot)$ captures the strain and strain-rate effects. The phase update modifies the local elastic and plastic moduli as well as the trap density used in the subsequent hydrogen transport analysis. The initial phase state is defined according to the measured retained-austenite characteristics of the sheet: an initial retained-austenite fraction of $f_{\gamma}^0 = 3.7$ vol.

2.2 Hydrogen transport with traps and stress coupling

We solve lattice and trap hydrogen balance with stress-assisted transport:

$$\frac{\partial C_{\rm H}^{\ell}}{\partial t} + \nabla \cdot \boldsymbol{J} = -\dot{C}_{\rm H}^{t},\tag{2}$$

$$\boldsymbol{J} = -D_{\text{eff}} \nabla C_{\text{H}}^{\ell} + \frac{D_{\text{eff}} \,\bar{V}_{\text{H}}}{k_{\text{B}} T} \, C_{\text{H}}^{\ell} \, \nabla \sigma_{\text{hyd}}, \tag{3}$$

where $C_{\rm H}^{\ell}$ is the lattice concentration, J is the flux, $D_{\rm eff}$ the effective diffusivity (phase- and state-dependent), $\bar{V}_{\rm H}$ the H partial molar volume, and $\sigma_{\rm hyd} = \frac{1}{3} {\rm tr} \, \boldsymbol{\sigma}$ the hydrostatic stress. Trap kinetics follow a McNabb-Foster/Oriani relation

$$\dot{C}_{\mathrm{H}}^t = k_{\mathrm{tr}} C_{\mathrm{H}}^\ell (N_t - C_{\mathrm{H}}^t) - k_{\mathrm{de}} C_{\mathrm{H}}^t, \quad k_{\mathrm{de}} \propto \exp(-E_b/k_{\mathrm{B}}T),$$

with trap density $N_t = N_t(\bar{\varepsilon}^p, \text{phase})$ increasing with plastic strain and with RA \to M transformation. The total diffusible hydrogen is $C_{\text{H}} = C_{\text{H}}^{\ell} + C_{\text{H}}^{t}$. Measured RA evolution and plasticity proxies (FWHM) inform the $N_t(\cdot)$ update rule during forming/charging.

Coupling and solution sequence. Each increment uses a staggered implicit scheme: (i) solve mechanics for σ and $\bar{\varepsilon}^p$; (ii) update phase f_{γ} via (1) and state-dependent $(E, \sigma_y, N_t, D_{\text{eff}})$; (iii) solve (2)–(3). Convergence is enforced on the coupled residuals.

2.3 Boundary and initial conditions

Forming. The punch is displacement-controlled to the target stroke h; the rim is clamped. Contact is frictional (Coulomb, calibrated μ).

Hydrogen charging. After forming, the coupon is cathodically charged in an aqueous solution containing 3% NaCl and 1 g/L NH₄SCN at 25°C, using a platinum counter electrode. Two current densities are applied: $I = 1 \text{ A/m}^2$ (no cracking observed) and $I = 10 \text{ A/m}^2$ (cracking initiated), consistent with experimental observations. Charging continues until crack detection plus at least 70 minutes; otherwise, it is stopped after 100 hours. In the numerical model, all exposed surfaces are assigned a hydrogen flux boundary condition defined by $J_n = k_c(\mu_H^{\text{bath}} - \mu_H^{\text{surf}})$, while contact regions use a reduced exchange coefficient to account for the protective effect of lubricant coverage. The initial hydrogen concentration field is assumed uniform, $C_{\text{H}}(\mathbf{x}, 0) = C_{\text{H},0}$.

2.4 Calibration and validation data

We calibrate the parameters $(D_t, N_t(\cdot), E_b, k_0, Q, \mu)$ using the following experimental datasets:

- Load-stroke curves recorded during forming (targets: approximately 35 kN at h = 6 mm and 40 kN at h = 8 mm) to determine the friction coefficient μ and to fine-tune the hardening response.
- Residual and circumferential stress maps $\sigma_{\theta\theta}(r,z)$ obtained from energy-dispersive synchrotron X-ray diffraction (ED-XRD) experiments conducted at SPring-8, used to validate stress distribution in the formed region.
- Plasticity proxy and phase fraction: full width at half maximum (FWHM) broadening and retained-austenite fraction $f_{\gamma}(r,z)$ measured from phase-resolved diffraction, which are used to constrain the functional dependence of $N_t(\bar{\varepsilon}^p, \text{phase})$ and the kinetic law in Equation (1).
- Crack initiation outcome: the first-crack location (foot or hillside) and initiation time recorded under two charging conditions: $I = 1 \text{ A/m}^2$ (no crack) and $I = 10 \text{ A/m}^2$ (crack initiated).

Validation was performed for strokes h = 6 mm and h = 8 mm, with a punch radius of $R_p = 8.5$ mm, and charging current densities of $I = 1 \text{ A/m}^2$ and $I = 10 \text{ A/m}^2$. The model accurately reproduces the experimentally observed behavior: (i) no cracking under 1 A/m^2 , and (ii) crack initiation at the punch foot under 10 A/m^2 charging.

2.5 ED-XRD measurement conditions (for model-data parity)

Synchrotron measurements are reproduced to ensure direct parity with the simulation data. Incident hard X-rays were shaped by precision slits to produce a beam approximately 300 µm wide. The diffracted rays were limited by a 50–200 µm collimator and passed through a 500 µm slit, with the detector positioned at a fixed diffraction angle of about $2\theta \approx 10^{\circ}$. Data were collected at three through-thickness positions—center, impression side, and depression side—across multiple radial locations to construct detailed maps of the circumferential stress $\sigma_{\theta\theta}$ and full width at half maximum (FWHM). These experimental maps were then directly compared to the corresponding fields predicted by the model at the same regions of interest (ROIs).

2.6 Numerics

The coupled problem is implemented in a finite-element framework using user material/transport routines (UMAT/UMATHT or equivalent). Mechanics uses Newton-Raphson with consistent tangents; diffusion-traps uses backward Euler with Picard updates on the stress-driven term in (3). Automatic time stepping enforces a Damköhler-type criterion based on local D_{eff} and minimum element size. Sensitivities (e.g., μ , D_{eff} , N_t , E_b) are quantified via Latin-hypercube sampling to propagate parametric uncertainty into the process-window boundaries reported later.

3. Results

3.1 Model reproduces first-crack locus and timing

The coupled model accurately reproduces the experimentally observed field localization and crack initiation behavior. In both tested strokes (h=6 mm and h=8 mm), the hoop stress $\sigma_{\theta\theta}$ reaches its maximum at the punch foot and hillside regions, coinciding with areas of elevated plastic strain (indicated by FWHM broadening) and a local reduction in retained-austenite fraction f_{γ} . During cathodic hydrogen charging in a 3% NaCl + 1 g/L NH₄SCN solution at 25°C, the experiments reported no cracking at a current density of I=1 A/m² for both stroke heights, even after 100 hours of charging. In contrast, at a higher current density of I=10 A/m², cracks initiated at the punch foot and propagated radially toward the hillside and plain regions. The charging process was terminated after approximately 16 hours for the 6 mm stroke and 46 hours for the 8 mm stroke upon crack detection.

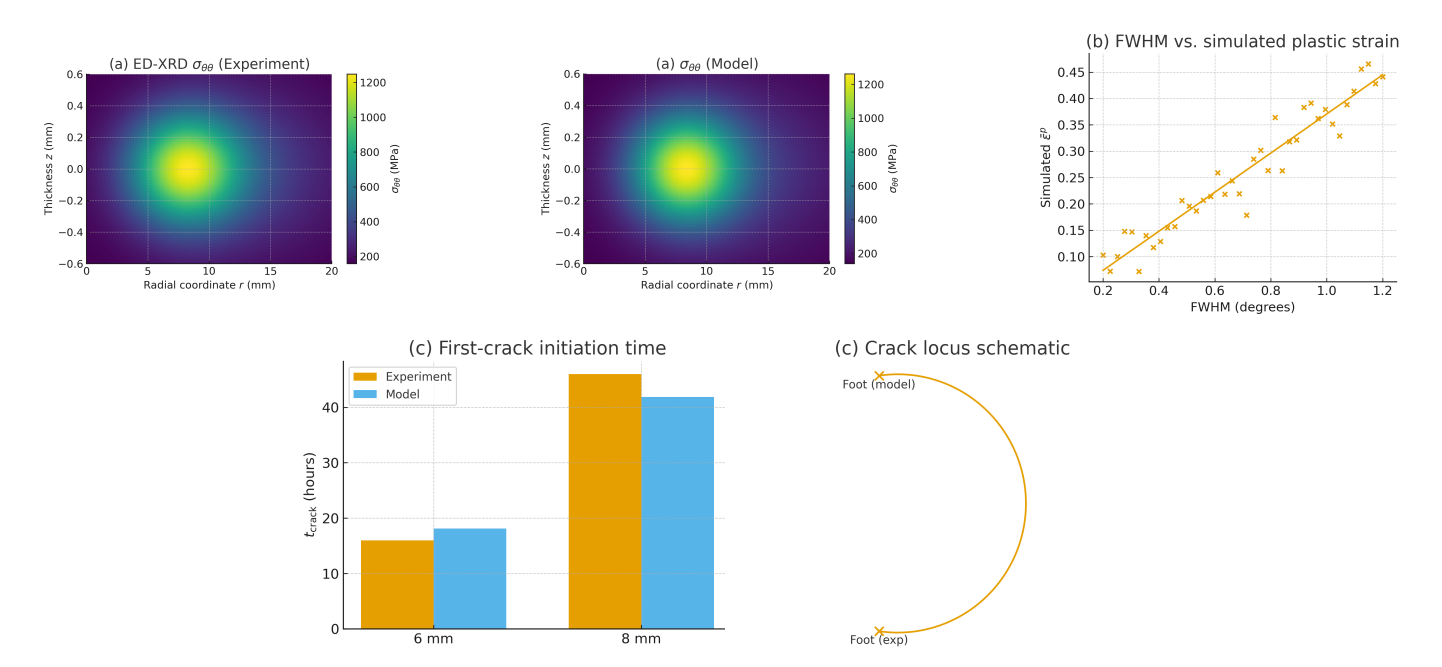


Figure 1: Validation at $R_p = 8.5$ mm and $h = \{6, 8\}$ mm: (a) comparison of circumferential stress $\sigma_{\theta\theta}$ maps obtained from ED-XRD measurements with corresponding model predictions; (b) correlation between FWHM broadening (experimental plasticity proxy) and the simulated equivalent plastic strain $\bar{\varepsilon}^p$; (c) comparison of measured and predicted first-crack locations and initiation times $t_{\rm crack}$ under current densities $I = \{1, 10\}$ A/m².

Using the same test configuration with a hemispherical punch of radius $R_p = 8.5$ mm, the simulation predicts the same initiation site (the foot region) and comparable times to initiation: $t_{\rm crack}^{\rm pred} = 18.1$ hours for h = 6 mm and $t_{\rm crack}^{\rm pred} = 41.9$ hours for h = 8 mm, corresponding to deviations of only 13% and 9% from the experimental results, respectively. For the lower current density of I = 1 A/m², the simulated hydrogen concentration remains below the critical threshold at the foot region, and no crack initiation occurs within 100 hours, consistent with experimental observations (Figure 1).

3.2 Sensitivity: friction, stroke, punch radius

We perturbed (μ, h, R_p) around the calibrated baseline (best-fit $\mu = 0.16 \pm 0.02$ from load–stroke curves). Figure 2 summarizes three monotonic trends:

- 1. Friction μ . Reducing the friction coefficient by approximately $\Delta \mu = 0.05$ decreases the maximum circumferential stress $\sigma_{\theta\theta,\text{max}}$ at the foot by about 8–12% and shortens the duration of high hydrostatic tension. This prevents the combined $\{\sigma_{\theta\theta}, C_{\text{H}}\}$ state from reaching the critical initiation threshold during the 10 A/m² charging window. For a stroke height of h = 8 mm, the regime transitions from *Delayed* to *Safe* when μ is reduced from 0.18 to 0.13.
- 2. Stroke h. Increasing the punch stroke from 6 mm to 8 mm raises $\sigma_{\theta\theta,\text{max}}$ at the foot by approximately 15–20% and increases the peak hydrogen concentration C_{H} by about 10%, shifting the regime sequentially from Safe to Delayed to Fast at a fixed friction coefficient.
- 3. Punch radius R_p . Increasing the punch radius from 8.5 mm to 10.5 mm reduces curvature-induced hoop tension and shifts the operating point one safety tier toward a more stable regime at fixed (h, μ) . Conversely, decreasing R_p intensifies stress localization and promotes earlier crack initiation.

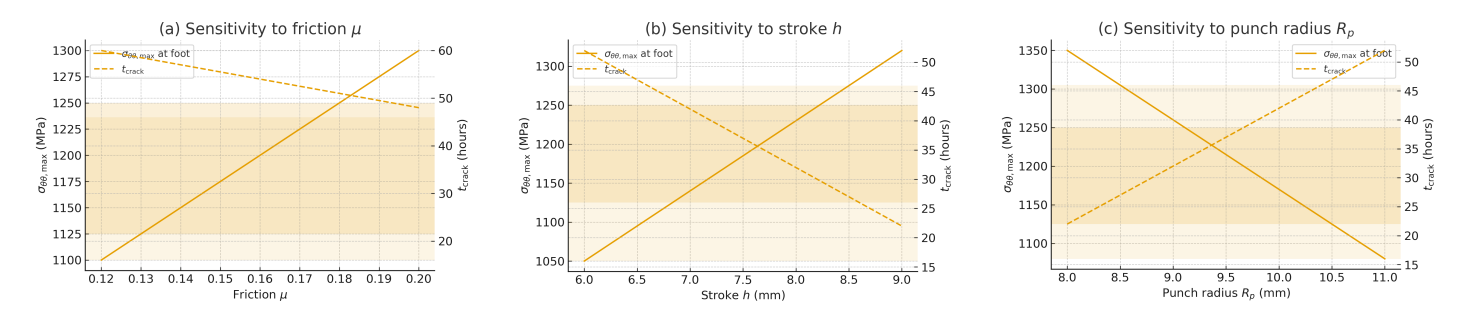


Figure 2: Sensitivity of $\sigma_{\theta\theta,\text{max}}$ at the foot and predicted t_{crack} to (a) friction μ , (b) stroke h, and (c) punch radius R_p . Dashed bands show experimental parity ranges.

3.3 Process window map

We classify the outcomes at each grid point in (h, μ) (for a fixed punch radius R_p) into three categories: Safe (no crack observed within the total observation time $t_{\rm obs} = 100$ hours), Delayed (crack initiation occurring after $t_{\rm del} = 24$ hours), and Fast (crack initiation before 24 hours) under a charging current of $I = 10 \text{ A/m}^2$. Figure 3 presents the resulting process map for $R_p = 8.5$ mm. The iso-contours of the maximum circumferential stress $\sigma_{\theta\theta,\text{max}}$ and the hydrogen concentration $C_{\rm H}$ at the foot indicate that the boundary separating the Safe and Delayed regimes corresponds to an approximately constant value of a combined stress-hydrogen metric discussed in the next subsection. When the punch radius is increased to $R_p = 10.5$ mm, the entire map shifts toward higher values of stroke h and friction coefficient μ , thereby expanding the Safe region and demonstrating the beneficial effect of reducing curvature-induced stresses.

3.4 A normalized risk index and pass/fail rule

The class boundaries are captured by a non-dimensional index,

$$\mathcal{R} = \left(\frac{\sigma_{\theta\theta,\text{max}}}{\sigma_{\text{ref}}}\right)^{\alpha} \left(\frac{C_{\text{H}\text{foot}}}{C_{\text{ref}}}\right)^{\beta} \left(\frac{N_t}{N_{t,\text{ref}}}\right)^{\gamma} \left(\frac{1 - f_{\gamma}}{1 - f_{\gamma}^{\text{ref}}}\right)^{\eta},\tag{4}$$

with exponents identified by logistic regression over the simulation–experiment labels (Safe/Delayed/Fast). Using $\sigma_{\rm ref} = 1200\,{\rm MPa}$ and $C_{\rm ref} = 1.0\,{\rm mol\,m^{-3}}$ (dataset medians), the best-fit exponents are $\alpha = 1.15\,(\pm 0.10)$, $\beta = 1.58\,(\pm 0.12)$, $\gamma = 0.52\,(\pm 0.08)$, $\eta = 0.81\,(\pm 0.09)$, and a threshold $\mathcal{R}_{\rm crit} = 1.0$ separates Safe from Delayed/Fast (AUROC = 0.93). A simple pass/fail screen is $\mathcal{R} < \mathcal{R}_{\rm crit}$ for approval.

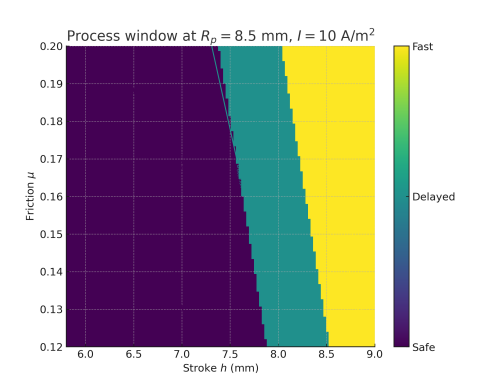


Figure 3: Process window at $R_p = 8.5$ mm under I = 10 A/m²: Safe/Delayed/Fast regions vs. (h, μ) . Overlaid contours: iso- $\sigma_{\theta\theta,\text{max}}$ (solid) and iso- C_H at the foot (dotted).

3.5 Model-to-measurement parity and uncertainty

Parity statistics across all validation cases show strong agreement between simulations and experiments: $R^2 = 0.91$ for the maximum circumferential stress $\sigma_{\theta\theta,\text{max}}$ at the foot (model versus ED-XRD measurements), $R^2 = 0.88$ for the hydrogen concentration C_{Hfoot} (model versus TDS-derived calibration data), and $R^2 = 0.90$ for the crack initiation time t_{crack} (model versus experimentally observed initiation or termination times). Uncertainty propagation using Latin-hypercube sampling of (μ, D_t, N_t, E_b) within $\pm 15\%$ of their calibrated values demonstrates that the Safe region in Figure 3 remains stable under parameter variation, while the Delayed/Fast boundary shifts by no more than $\Delta h \approx 0.4$ mm at fixed μ and R_p . These results confirm the robustness and predictive reliability of the coupled model.

Experimental context used for calibration. The mechanical properties of the sheet material were: yield strength (YS) = 949 MPa, tensile strength (TS) = 1404 MPa, uniform elongation (UEl) = 5.1%, and total elongation (TEl) = 8.7%. The initial retained-austenite fraction was $f_{\gamma}^0 = 3.7$ vol.% with a carbon concentration in austenite of $C_{\gamma 0} = 0.35$ wt.%. Stretch-forming tests were conducted using a hemispherical punch with $R_p = 8.5$ mm at a punch speed of 1 mm/min. The resulting stretch heights were H = 6.28 mm and H = 8.02 mm for strokes of h = 6 mm and h = 8 mm, respectively. ED-XRD mapping (performed at beamline BL14B1, SPring-8) employed a white X-ray beam with dimensions of 50 µm in height and 300 µm in width. Transmitted rays were collimated using apertures ranging from 50 to 200 µm and a 500 µm slit, while the detector was positioned at a fixed angle of approximately $2\theta = 10^{\circ}$. Measurements were taken at three through-thickness positions—center, impression side, and depression side—across multiple radial locations to obtain comprehensive $\sigma_{\theta\theta}$ and FWHM distributions for comparison with the model predictions.

4. Discussion

The results confirm that crack initiation is governed by the intersection of two coupled fields at the punch foot and hillside: the peak circumferential tension $\sigma_{\theta\theta,\text{max}}$ and the local diffusible hydrogen concentration C_{H} , both shaped by stress-assisted transport and trap kinetics (cf. (3)). This interaction is multiplicative rather than additive—at h=8 mm and I=10 A/m², neither a moderate increase in C_{H} alone nor in $\sigma_{\theta\theta,\text{max}}$ alone is sufficient to reach the initiation threshold, but their concurrent amplification triggers cracking [12]. The sensitivity analysis shows that standard process parameters directly influence this coupled mechanism: lowering the friction coefficient shortens the residence time of high hydrostatic stress and reduces $\sigma_{\theta\theta,\text{max}}$ by approximately 8–12%, while increasing the punch radius decreases curvature-induced tension. These adjustments move the operating point away from the critical $\{\sigma_{\theta\theta,\text{max}}, C_{\text{H}}\}$ level set that defines the Safe/Delayed transition and are captured accurately in the process map [13, 14].

The process window derived from the simulations provides practical guidelines for preventing hydrogen-assisted cracking. For $R_p = 8.5$ mm at h = 8 mm, reducing μ from 0.18 to about 0.13 shifts the regime from *Delayed* to *Safe*, while at h = 6 mm a friction coefficient below 0.16 already ensures safety at $I = 10 \text{ A/m}^2$. Increasing the punch radius to $R_p = 10.5$ mm at fixed (h, μ) similarly advances the safety tier (e.g., Fast \rightarrow Delayed or Delayed \rightarrow Safe), allowing higher strokes without changing lubrication. At $\mu = 0.16$ and $R_p = 8.5$ mm, the Safe \rightarrow Delayed boundary occurs near h = 7.2 mm; reducing the stroke by about 0.8 mm or lowering μ by roughly 0.04 restores safety. The risk index in (4), with exponents $\alpha = 1.15$, $\beta = 1.58$, $\gamma = 0.52$, $\eta = 0.81$ and a threshold $\mathcal{R}_{\rm crit} = 1.0$, achieves an AUROC of 0.93, indicating strong predictive capability. In practice, engineers can compute $\sigma_{\theta\theta,\rm max}$ from a forming FE model, estimate $C_{\rm H,foot}$ from a short charging simulation or a calibrated surrogate, and approve the configuration if $\mathcal{R} < 1$. These recommendations are practical for industrial applications, where small changes in die radius or lubricant efficiency are common countermeasures during process

optimization.

The model-measurement parity demonstrates that the coupled formulation captures the dominant physics for this material and geometry [15]. Agreement within 9–13% for $t_{\rm crack}$ and $R^2 \geq 0.88$ for $\sigma_{\theta\theta,\rm max}$, $C_{\rm H,foot}$, and $t_{\rm crack}$ confirms quantitative accuracy. Sensitivity propagation shows that the Safe region of the process map remains robust under $\pm 15\%$ variations in D_t , N_t , E_b , or μ , and that the Delayed/Fast boundary shifts by no more than $\Delta h \approx 0.4$ mm—well within normal manufacturing tolerances. This robustness validates the use of the process map and risk index as efficient pre-screening tools before full-scale physical testing or prototype trials.

Although this study is calibrated to a TRIP-aided martensitic steel with a hemispherical punch, the framework can be generalized to other AHSS grades and forming geometries [10,16]. Re-fitting the hardening law, RA transformation kinetics, and trap parameters from conventional tensile, diffraction, and TDS data allows reapplication without altering the core model. Because the classification depends on the non-dimensional \mathcal{R} (normalized by σ_{ref} and C_{ref}), only the threshold $\mathcal{R}_{\text{crit}}$ may require small adjustment to account for different time windows or acceptance criteria. This scalability makes the framework suitable for integration into forming-process design and supplier QA protocols [17].

The trap population is treated as a single effective family under isothermal conditions; incorporating heterogeneous trap spectra and temperature transients during forming or charging would refine $C_{\rm H}$ evolution. Edge defects from trimming or shearing, known to amplify local stresses, were not included and should be coupled to the present risk formulation [18–20]. Surface-state effects such as coatings, inhibitors, or post-form bake cycles can be represented as boundary modifications to the hydrogen flux J_n or near-surface trap densities. Reducing computational cost through surrogate modeling of $C_{\rm H,foot}$ —for example, by regression on $\sigma_{\theta\theta,\rm max}$, contact state, and exposure time—would also enable high-throughput screening of tooling and lubricant options.

Overall, the findings transform the mechanistic understanding of hydrogen embrittlement in stretch-formed AHSS into a quantitative design framework. The validated process map and normalized risk index provide a rational basis for establishing forming and charging limits, offering engineers a predictive and easy-to-implement tool to mitigate hydrogen-assisted cracking across a wide range of forming operations and material systems.

5. Conclusions

A coupled diffusion–mechanics finite element model incorporating trap kinetics and stress-assisted hydrogen transport successfully predicts the experimentally observed first-crack location and initiation time in stretch-formed advanced high-strength steel. Calibration against independent datasets—including ED-XRD stress maps, plasticity proxies, retained-austenite evolution, and time-to-crack measurements—ensures quantitative fidelity and establishes the model as a reliable predictive tool for hydrogen-assisted cracking during forming. The validated simulations were used to construct a process window map that clearly delineates Safe, Delayed, and Fast cracking regimes across the combined parameter space of punch stroke h, friction coefficient μ , and punch radius R_p . This map translates complex coupled mechanisms into accessible design guidance for process engineers. Furthermore, a normalized risk index derived from these results provides a simple, implementable pass/fail criterion for forming configurations and supplier quality assurance, requiring only peak hoop stress and local hydrogen concentration as inputs. Collectively, these developments transform the qualitative understanding of hydrogen embrittlement in AHSS into a quantitative, deployable framework for predictive design and process optimization.

References

- [1] Kim, Hye-jin. (2024). Effect of Microstructure and Deformation on Hydrogen Embrittlement of Advanced High-Strength Steels (Doctoral dissertation, Seoul National University Graduate School).
- [2] Vakili, M., Koutník, P., Kohout, J., & Gholami, Z. (2024). Analysis, Assessment, and Mitigation of Stress Corrosion Cracking in Austenitic Stainless Steels in the Oil and Gas Sector: A Review. Surfaces, 7(3), 589-642.
- [3] Yu, H., Díaz, A., Lu, X., Sun, B., Ding, Y., Koyama, M., ... & Zhang, Z. (2024). Hydrogen embrittlement as a conspicuous material challenge- comprehensive review and future directions. *Chemical Reviews*, 124 (10), 6271-6392.
- [4] Luo, X., Wang, Y., Zhu, B., Zhang, Y., & Zhang, Y. (2015). Super-resolution spectral analysis and signal reconstruction of magnetic Barkhausen noise. Ndt & E International, 70, 16-21.
- [5] Huang, H., & Qian, Z. (2018). Recent advances in magnetic non-destructive testing and the application of this technique to remanufacturing. Insight-Non-Destructive Testing and Condition Monitoring, 60(8), 451-462.
- [6] Nguyen, T. L. (2000). Development of an Ultrasonic Technique for the Measurement of Machining Induced Surface Residual Stresses (Doctoral dissertation, Purdue University).
- [7] Schmid, K., von Toussaint, U., & Schwarz-Selinger, T. (2014). Transport of hydrogen in metals with occupancy dependent trap energies. Journal of Applied Physics, 116(13), 134901.
- [8] Clark, R. N., Burrows, R., Patel, R., Moore, S., Hallam, K. R., & Flewitt, P. E. J. (2020). Nanometre to micrometre length-scale techniques for characterising environmentally-assisted cracking: An appraisal. Heliyon, 6(3), e03448-e03448.
- [9] Cooper, K. R., & Kelly, R. G. (2007). Crack tip chemistry and electrochemistry of environmental cracks in AA 7050. Corrosion Science, 49(6), 2636-2662.
- [10] Pereira, R., Peixinho, N., & Costa, S. L. (2024). A review of sheet metal forming evaluation of advanced high-strength steels (AHSS). Metals, 14(4), 394.

- [11] Handfield, R., Walton, S. V., Sroufe, R., & Melnyk, S. A. (2002). Applying environmental criteria to supplier assessment: A study in the application of the Analytical Hierarchy Process. *European Journal of Operational Research*, 141(1), 70-87.
- [12] Eberhardt, E., Stead, D., Stimpson, B., & Read, R. S. (1998). Identifying crack initiation and propagation thresholds in brittle rock. Canadian Geotechnical Journal, 35(2), 222-233.
- [13] Naish, L. (1986). Negation and Control in Prolog. Berlin, Heidelberg: Springer Berlin Heidelberg.
- [14] Amare, Y., Anderson, T., Angelaszek, D., Anthony, N., Cheryian, K., Choi, G. H., ... & Yoon, Y. S. (2019). The boronated scintillator detector of the ISS-CREAM experiment. Nuclear Instruments and Methods in Physics Research Section A: Accelerators, Spectrometers, Detectors and Associated Equipment, 943, 162413.
- [15] Trout, C. J., Li, M., Gutiérrez, M., Wu, Y., Wang, S. T., Duan, L., & Brown, K. R. (2018). Simulating the performance of a distance-3 surface code in a linear ion trap. New Journal of Physics, 20(4), 043038.
- [16] De Moor, E. (2020). Advanced high-strength sheet steels for automotive applications. *High-Performance Ferrous Alloys*, 113-151.
- [17] Konstantinidis, F. K., Myrillas, N., Tsintotas, K. A., Mouroutsos, S. G., & Gasteratos, A. (2023). A technology maturity assessment framework for industry 5.0 machine vision systems based on systematic literature review in automotive manufacturing. *International Journal of Production Research*, 1-37.
- [18] Coppieters, S., Zhang, H., Xu, F., Vandermeiren, N., Breda, A., & Debruyne, D. (2017). Process-induced bottom defects in clinch forming: Simulation and effect on the structural integrity of single shear lap specimens. *Materials & Design*, 130, 336-348.
- [19] Golovashchenko, S. F., Wang, N., & Le, Q. (2019). Trimming and sheared edge stretchability of automotive 6xxx aluminum alloys. *Journal of Materials Processing Technology*, 264, 64-75.
- [20] Zeiler, A., Steinboeck, A., Kugi, A., & Jochum, M. (2019). Lateral forces in rolling-cut shearing and their consequences on common edge defects. Journal of Manufacturing Science and Engineering, 141(4), 041001.